Available online at www.sciencedirect.com
ScienceDirect
ELSEVIER
Journal of Solid State Chemistry 179 (2006) 3406–3419
JOURNAL OF SOLID STATE CHEMISTRY
www.elsevier.com/locate/jssc

# Cerium effect on the phase structure, phase stability and redox properties of Ce-doped strontium ferrates

F. Deganello[a,*], L.F. Liotta[a], A. Longo[a], M.P. Casaletto[a], M. Scopelliti[b]

[a]Istituto per lo Studio dei Materiali Nanostrutturati del C.N.R, Sezione di Palermo, Via Ugo La Malfa 153, 90146-Palermo, Italy
[b]Dipartimento di Chimica Inorganica e Analitica"S. Cannizzaro", Università di Palermo Parco d'Orleans, Viale delle Scienze, 90128-Palermo, Italy

Received 2 May 2006; received in revised form 5 June 2006; accepted 9 June 2006
Available online 29 June 2006

## Abstract

Nanostructured perovskite-type $Sr_{1-a}Ce_aFeO_{3-x}$, ($0 \leqslant a < 0.15$) powders have been prepared by citrate–nitrate smoldering auto-combustion. Their phase structure and stability, surface and morphological properties, reduction behavior and interaction with oxygen have been investigated by X-ray Powder Diffraction combined with Rietveld Analysis, $^{57}$Fe Mössbauer and X-ray Photoelectron Spectroscopies, $N_2$-adsorption method, Temperature Programmed Reduction and Oxidation experiments. Our results reveal that citrate–nitrate auto-combustion method is effective in obtaining single phase $Sr_{1-a}Ce_aFeO_{3-x}$. The $Sr_{1-a}Ce_aFeO_{3-x}$ structure is cubic only for $a \geqslant 0.06$, while for $a < 0.06$ remains tetragonal. Moreover, for $a \geqslant 0.06$ after semi-reductive treatment under inert gas, an expanded cubic phase is obtained instead of the brownmillerite-type structure, which is known to have ordered vacancies. Stabilization of octahedral $Fe^{3+}$ by cerium doping appears to be the main factor in determining the structural properties of $Sr_{1-a}Ce_aFeO_{3-x}$. The highest oxygen consumption for Ce-doped $SrFeO_3$ occurs for $a = 0.06$. Preliminary impedance measurements show that $Sr_{0.94}Ce_{0.06}FeO_{3-x}$ has the lowest area-specific resistance.

*Keywords:* Ce-doped strontium ferrates; Perovskite-type materials; Smoldering auto-combustion synthesis; Octahedral $Fe^{3+}$

## 1. Introduction

Strontium ferrates are strontium–iron mixed oxides with $ABO_3$ perovskite-type structure. Iron in strontium ferrates is found mainly as $Fe^{4+}$, but oxygen deficiency is usually present so that some $Fe^{3+}$, with larger ionic radius, is formed depending on the synthesis conditions. Pure and doped strontium ferrates have attracted much interest as sensors [1], magnetotransport [2,3] and oxygen permeation membrane materials [4]. Recently they have been studied for their mixed ionic–electronic conducting properties, which make them promising candidate materials for oxygen-conducting devices such as solid oxide fuel cell (SOFC) cathodes [5–7]. The large oxygen non-stoichiometry range that these perovskite materials are able to accommodate is an important factor to achieve high oxygen mobility values. It has been reported that strontium ferrates release large amounts of oxygen on heating in inert gas flow, after pre-adsorption of oxygen [8]. However, as the oxygen vacancy concentration increases, the probability of forming much less oxygen-conducting ordered structures also increases. For example, the brownmillerite-type structure $ABO_{2.5}$ can be obtained from the perovskite-type structure $ABO_3$ under inert gas treatment at high temperature [9]. The crystal structure of the brownmillerite-type phase is related to the perovskite phase: while the $ABO_3$ perovskite phase consists of $BO_6$ octahedra, the $ABO_{2.5}$ brownmillerite phase has $BO_6$ octahedra alternating with $BO_4$ tetrahedra along the *b*-axis, resulting in an orthorhombic symmetry, containing $Fe^{3+}$, with ordered oxygen vacancies. The orthorhombic brownmillerite-type phase transforms into higher oxygen-conducting cubic phase at $T > 800\,°C$, due to a thermal disordering of the oxygen vacancies [9]. Knowing the behavior of strontium ferrate in a large temperature and oxygen pressure range is of outmost importance for their application in SOFC and oxygen permeation membranes.

---

*Corresponding author. Fax: +39 091 6809399.
*E-mail address:* francesca.deganello@ismn.cnr.it (F. Deganello).

0022-4596/$ - see front matter © 2006 Published by Elsevier Inc.
doi:10.1016/j.jssc.2006.06.027

Proper substitution of the A or B site with metal cations may improve the phase and structure stability and oxygen permeability by affecting the iron oxidation state. Among the dopant cations investigated in literature, lanthanum has been reported to produce rhombohedral or tetragonal structure, depending on the dopant content, and to form brownmillerite structure after high-temperature treatment at low oxygen partial pressure [10]. Other authors reported a cubic structure for La-doped $SrFeO_3$, although their powders were prepared under high oxygen pressure thermal annealing [11]. On the contrary, Pr [12] and Bi-doped [4] $SrFeO_3$ are usually cubic or tetragonal, depending on the dopant content, and form expanded cubic perovskite-type structure after oxygen loss at low oxygen partial pressure. In contrast with other A-site-doped $SrFeO_3$, Ce-doped $SrFeO_3$ show some differences in the full stoichiometric structures: for example, while $BiFeO_3$ and $PrFeO_3$ do exist, $CeFeO_3$ can be obtained only in harsh reductive environments or by using particular synthesis condition [13]. To our knowledge, only few papers have been published on Ce-doped strontium ferrates [5,14,15]. In particular, Trofimenko and Ullmann [14] demonstrated the mixed ionic–electronic conductivity of $(Sr,Ce)(Fe,Co)O_{3-x}$ both by oxygen permeation and oxide ion and electronic conductivity measurements. They showed that a $Sr_{1-a}Ce_aFeO_{3-x}$ solid solution with a cubic structure forms for $a \leqslant 0.15$ by substituting $Sr^{2+}$ ion ($r_{Sr^{2+}} = 1.44$) with $Ce^{3+}$ ion ($r_{Ce^{3+}} = 1.34$). Cerium doping causes oxygen vacancies suppression and modifies some of the properties of strontium ferrates like oxygen and electronic conduction [14].

This paper describes the preparation and characterization of $Sr_{1-a}Ce_aFeO_{3-x}$ perovskite-type materials in order to find new structure–properties relationships and useful indications for the application of these materials in low-temperature oxygen-conducting devices. The preparation of the full range of $Sr_{1-a}Ce_aFeO_{3-x}$ perovskite-type mixed oxides was carried out by a citrate–nitrate smoldering auto-combustion method. The powder generally obtained by solution combustion methods has an higher degree of phase purity with improved powder characteristics, such as narrow crystal size distribution, nanometer-sized particles, high surface area and good sinterability [16]. All these features may dramatically affect both the electronic and ionic transport properties, leading to improved performances [17]. The structure of the Ce-doped strontium ferrate powders has been studied by X-ray powder diffraction (XRD) combined with Rietveld analysis; the iron electronic environment by Mössbauer measurements; surface area and pore distribution by $N_2$ absorption method; surface modifications by X-ray photoelectron spectroscopy (XPS) and the redox properties by temperature programmed reduction (TPR) and oxidation (TPO) experiments. Preliminary electrochemical impedance spectroscopy (EIS) measurements have been also performed to get a first insight of the cerium effect on the electrochemical performance of these compounds as cathodes for oxygen reduction.

## 2. Experimental procedure

### 2.1. Powders preparation

For the preparation of the powdered samples, a method based on the citrate–nitrate auto-combustion has been employed. A detailed description of the powder preparation will be published in a forthcoming paper [18]. Briefly, stoichiometric amounts of strontium nitrate (Carlo Erba $\geqslant$ 99.0%), iron nitrate (Carlo Erba 98%) and cerium nitrate (Sigma Aldrich 99.99%) have been dissolved in distilled water. Then citric acid (Merk 99%), in a twofold molar excess of the total metal ions, has been dissolved into the metal nitrates solution and the pH of the resulting mixture has been adjusted to 9 by $NH_3$ solution (30%). Finally ammonium nitrate (Merk $\geqslant$99%), has been added to obtain a citrate/nitrate ratio of 0.46. The combustion process is mainly regulated by this ratio, where citrate is the fuel, whereas nitrates, coming from metal precursors and from ammonium nitrate, are the oxidants.

The combustion of the homogeneous solution has been carried out in a high-temperature silicon oil bath. The water has been evaporated at 70 °C under constant mechanical stirring, until a green gel was obtained. The temperature of the bath has been then gradually raised to 200 °C until self-ignition. The spontaneous combustion lasted for about 10–20 s resulting in a fluffy powder. This powder has been then fired in stationary air at 1000 °C for 4 h. The powders obtained after firing at 1000 °C have been named "as prepared powders". In this paper, $Sr_{1-a}Ce_aFeO_{3-x}$ perovskite-type materials are designated by the abbreviation SFC followed by a number that refers to the nominal Ce molar percentage in the material.

### 2.2. Powders characterization

X-ray diffraction measurements have been carried out on a PHILIPS PW1830 X-ray powder diffractometer using Ni-filtered Cu $K_\alpha$ radiation (40 kV/40 mA). A step size of $0.05°2\theta$, an integration time of 3 s per step and a scan range from 20 to $98°2\theta$ were used. The diffraction patterns have been analyzed by Rietveld refinement using the GSAS package [19]. Chebyschev polynomials and Pearson VII functions have been chosen for the background and for the peak profile fitting, respectively. In the structure refinement, lattice constants, Debye Waller factors, microstrain and full width half maximum (FWHM) have been considered as variables parameters. For all the fitting analysis [20], parameters have been considered. From fitting results, the structural parameters of the investigated compounds and, in particular, the cell edge lengths and the relative phase composition were obtained. Thermal parameters were optimized and their values were found in good agreement with the literature. The agreement factors, reported in the tables as quality indicators for the goodness of the Rietveld fitting, are the weighted-profile value ($wR_p$), the expected profile value ($R_p$) and the Bragg-intensity value ($R_F^2$), whose detailed definitions are given elsewhere in the literature [20]. All the agreement factors are expressed as percentage values and they should be lower than 10%. An estimation of the crystal size values has been obtained from Sherrer equation in agreement with the GSAS package procedure.

$^{57}$Fe Mössbauer spectra have been collected by a conventional spectrometer with triangular drive signal (FG2 function generator and MR250 velocity transducer, München Wissenschaftliche Elektronik Germany; proportional Kr/CH$_4$ counter, ADC 1683; memory unit/multichannel analyzer 269, Takes, Italy). For all experiments, a $^{57}$Co/Rh source (10 mCi, Ritverc GmbH, Russian Federation) has been used. The velocity calibration has been done by measuring the hyperfine splitting of $\alpha$-$^{57}$Fe foil (4 μm, Ritverc GmbH). All isomer shifts are referred to $\alpha$-Fe. Spectra have been evaluated using Lorentz and Voigt lineshapes in a non-linear MEM curve fitting software. Since the temperature dramatically influences the oxygen content of the samples, and thus their structure and geometry [21], only room temperature (RT) spectra were collected.

XPS analysis has been performed by a VG Microtech ESCA 3000 Multilab spectrometer, equipped with a standard Al $K_\alpha$ excitation source ($hv = 1486.6$ eV), a nine-channeltrons detection system and an electron hemispherical analyzer operating at a constant pass energy of 20 eV. The binding energy (BE) scale has been calibrated by measuring C 1*s* peak (BE = 285.1 eV) from the ubiquitous surface layer of adventitious carbon. The accuracy of the BEs location is ±0.1 eV. A non-linear least-square peak fitting routine has been used for the analysis of XPS spectra, separating elemental species in different oxidation states, after a Shirley [22] background subtraction from all the spectra. Relative concentrations of chemical elements have been calculated by a standard quantification routine, including Wagner's energy dependence of attenuation length [23] and a standard set of VG Escalab sensitivity factors.

Surface area (BET method) [24] and mesopore size distributions (BJH method) [25] have been determined by nitrogen adsorption/desorption measurements at 77 K, using a Sorptomatic 1900 Carlo Erba Instrument. A pre-treatment under vacuum at 250 °C for 1.5 h has been used.

Reduction properties of the perovskite oxides have been studied by TPR measurements. Experiments have been carried out with a Micromeritics Autochem 2910 apparatus, equipped with a thermal conductivity detector and a mass quadrupole (Thermostar$^{TM}$, Balzers). A weighted portion of the samples of about 100 mg has been pre-treated in a quartz reactor in 5% O$_2$ in He (30 mL/min) at 500 °C for 1 h, followed by purging and cooling to RT in Ar flow. Then, the flow has been switched to the mixture 5% H$_2$ in Ar (30 mL/min) and the temperature has been increased linearly up to 1000 °C (rate of 10 °C/min). In order to investigate the effects of sample aging on the reduction properties of the samples, the TPR experiment has been repeated twice, after a reoxidation at 1000 °C (rate of 10 °C/min) and He cooling. The standard deviation for the overall hydrogen uptake is ±15% and the error on the peak temperature is ±15 °C.

TPO experiments have been performed after temperature programmed desorption (TPD) pre-treatment. TPD pre-treatment has been carried out in He flow by heating up the as-prepared powders to 1000 °C and cooling them down to RT in He flow. In a typical TPO experiment, immediately after the TPD pre-treatment, the powder was heated from RT to 1000 °C by flowing O$_2$(5%)/He (30 mL/min) until 1000 °C. In order to check the reversibility of process, the TPD–TPO cycle has been repeated twice.

### 2.3. EIS characterization

Preliminary EIS measurements have been performed on symmetric cells of $Sr_{1-a}Ce_aFeO_{3-x}$ ($a = 0, 0.06, 0.15$) on a $Ce_{0.8}Sm_{0.2}O_{2-x}$ electrolyte to investigate the effect of Ce doping on the area-specific resistance (ASR).

Dense electrolyte pellets for impedance measurements have been prepared by weighting 0.8 g of $Ce_{0.8}Sm_{0.2}O_{2-x}$ powders, prepared by citrate–nitrate auto-combustion method, and by forming the powders by uniaxially pressing (2 tons for 1 min). A final diameter of ≈11 mm and a thickness of ≈1.4 mm have been obtained. Pellets have been pre-sintered at 1100 °C for 5 h and then further sintered for 10 h at 1500 °C. The pellet surfaces have been carefully polished before the electrode deposition.

SFC powders have been mixed with PEG (MW 400) and ethanol. Then homogenization has been ensured by mixing for 30 min in an ultrasonic bath. Alcohol evaporation has been performed in an oven at 80 °C. Coating of the electrodes on the electrolyte has been performed by screen printing of the SFC powder pre-sintered at 1000 °C. After coating the first side of the pellet, the pellet has been left for 30 min at 160 °C to dry the coating layer. Then the other side has been coated and dried again at 160 °C. The sintering temperature has been set to 1000 °C for 1 h.

EIS measurements have been carried out in the 600–800 °C temperature range using a frequency response analyzer (FRA, Solartron 1260 Impedance/Gain-phase) coupled with a dielectric interface (Solartron 1296), with an AC amplitude of 10 mV in the frequency range from 0.01 Hz to 13 MHz. Electrical current collectors have been made of gold wires on one side and a net on the other side to ensure contact area between gold and cathodes. The interfacial resistance of cathodes has been measured in the two-electrode symmetric cell configuration under air.

## 3. Results and discussion

### 3.1. As-prepared powders

Phase composition and structure of the as-prepared samples have been determined by XRD after firing at 1000 °C. In order to investigate cerium effect on strontium ferrates structure, an accurate Rietveld analysis on the XRD data has been performed and the results are summarized in Table 1.

Fig. 1 shows some representative Rietveld fittings. In this work, the undoped strontium ferrate (SF) has a tetragonal $I4/mmm$ structure (Fig. 1a,d), similar to $Sr_8Fe_8O_{23}$ already

Table 1
Rietveld refinement results for $Sr_{1-a}Ce_aFeO_{3-x}$ samples with different Ce content

| Sample name | Phase composition[a] (% wt) | XRD space group (structure) Cell parameters [b] (Å) | Crystal size (nm) | Agreement factors (%) |
|---|---|---|---|---|
| SF | $Sr_8Fe_8O_{23}$ (100) | $I4/mmm$ (tetragonal)<br>$a_0 = b_0 = 10.932$; $c_0 = 7.701$ | 248(20) | $wR_p = 1.74$<br>$R_p = 1.22$<br>$R_F^2 = 8.68$ |
| SFC2 | $Sr_{0.98}Ce_{0.02}FeO_{3-x}$(100) | $P4/mmm$ (tetragonal)<br>$a_0 = b_0 = 3.864$<br>$c_0 = 3.854$ | 115(5) | $wR_p = 2.13$<br>$R_p = 1.39$<br>$R_F^2 = 8.14$ |
| SFC6 | $Sr_{0.94}Ce_{0.06}FeO_{3-x}$ (100) | $Pm-3m$ (cubic)<br>$a_0 = b_0 = c_0 = 3.872$ | 92(5) | $wR_p = 2.21$<br>$R_p = 1.45$<br>$R_F^2 = 5.72$ |
| SFC10 | $Sr_{0.90}Ce_{0.10}FeO_{3-x}$ (100) | $Pm-3m$ (cubic)<br>$a_0 = b_0 = c_0 = 3.877$ | 101(5) | $wR_p = 2.11$<br>$R_p = 1.37$<br>$R_F^2 = 3.68$ |
| SFC15 | $Sr_{0.85}Ce_{0.15}FeO_{3-x}$ (99.0(2))<br>$CeO_2$ (<1) | $Pm-3m$ (cubic)<br>$a_0 = b_0 = c_0 = 3.884$ | 89(5) | $wR_p = 1.86$<br>$R_p = 1.30$<br>$R_F^2 = 5.39$ |
| SFC25 | $Sr_{0.85}Ce_{0.15}FeO_{3-x}$ (91.8(3))<br>$CeO_2$ (8.2(1)) | $Pm-3m$ (cubic)<br>$a_0 = b_0 = c_0 = 3.884$ | 70(5) | $wR_p = 2.21$<br>$R_p = 1.52$<br>$R_F^2 = 4.73$ |

[a] "$a$" values are deduced from the nominal Ce content and from the phase composition.
[b] Standard deviation for cell parameters is ±0.003 Å.

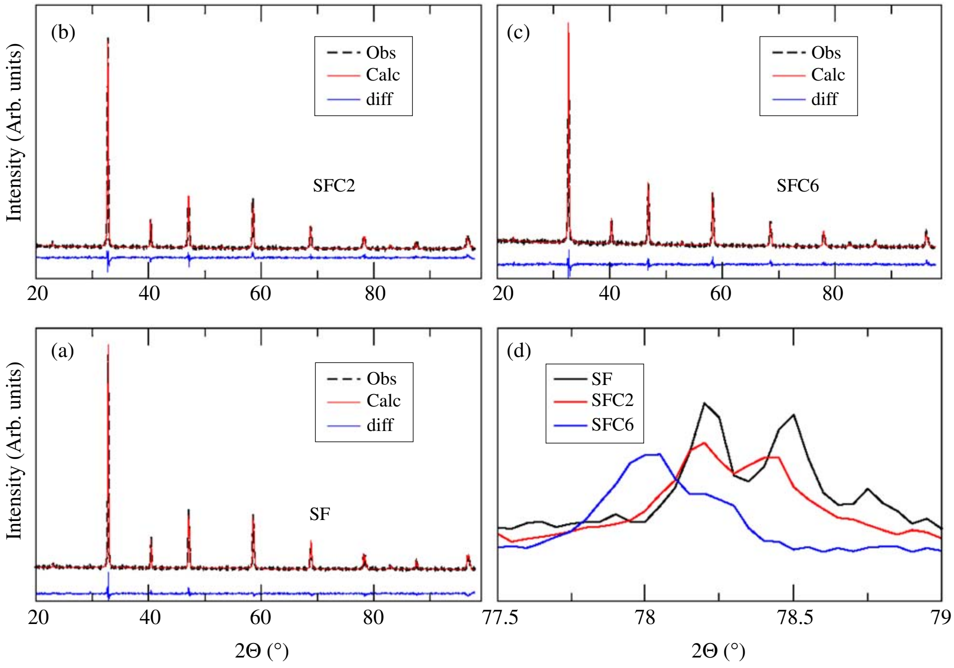

Fig. 1. Representative XRD structures of fresh Ce-doped strontium ferrates: (a) Rietveld refinement of SF with $I4/mmm$ structure; (b) Rietveld refinement of SFC2 XRD pattern with P $4/mmm$ structure; (c) Rietveld refinement of SFC6 XRD pattern with $Pm-3m$ structure; (d) enlargement of the SF, SFC2 and SFC6 XRD patterns with different structures.

described in literature [26]. It is already known in the literature that undoped strontium ferrates ($SrFeO_{3-x}$) may have different XRD structures depending on their oxygen stoichiometry [26], which is in turn determined by the synthesis conditions. The more the oxygen content, the more symmetric the structure, i.e. for a minimum oxygen content ($x = 0.5$), the structure is orthorhombic, whereas for a maximum oxygen content ($x = 0$) the structure is pure cubic. An intermediate oxygen content is usually obtained, whereas the extreme oxygen content can be obtained only in particular synthesis conditions [26].

For a 2 mol % Ce content (SFC2), the XRD pattern can be well described by a tetragonal *P*4/*mmm* structure with $c_0/a_0 < 1$ (Fig. 1b,d), as already found for $Sr_{0.9}Bi_{0.1}FeO_{3-x}$ [27]. For a Ce content $\geqslant$6 mol%, a cubic *Pm*3*m* structure forms, as shown for the SFC6 sample in Fig. 1c and Fig. 1d. The same cubic structure for Ce-doped strontium ferrates was found by Trofimenko and Ullmann [14], although they reported cubic structures for the whole range of dopant content. This discrepancy is probably due to the different preparation and sintering conditions used by these authors [14].

By increasing the cerium content in $Sr_{1-a}Ce_aFeO_{3-x}$, the cell parameter increases, as indicated by the shift of the diffraction peak toward lower angles in Fig. 2a. For higher cerium content, a $CeO_2$ phase segregates, as clearly shown by the phase composition of the most concentrated sample (SFC25) in Table 1. Due to no weight loss during the spontaneous combustion and formation of single-phase perovskite, the SFC stoichiometry ("*a*" value), which has been reported in Table 1, has been assumed to be that of the metal nitrates precursors in the starting solution, except for SFC15 and SFC25, where some segregated $CeO_2$ is also present and "*a*" value corresponds to the maximum cerium solubility. Fig. 2b shows that a linear correlation between cell volume (normalized to the number of atoms in the cell unit) and cerium nominal content exists until 15 mol%, in good agreement with literature results [14]. From these results, the limit of Ce solubility in $Sr_{1-a}Ce_aFeO_{3-x}$ corresponds to 14–15 mol%. This value is very close to that already found by Trofimenko and Ullmann [14].

The cell expansion observed for increasing Ce content can be ascribed to the formation of $Fe^{3+}$ cations, with higher ionic radius ($r_{Fe^{3+}} = 0.645$ [28]) than $Fe^{4+}$ ($r_{Fe^{4+}} = 0.585$ [28]). $Fe^{3+}$ formation has been confirmed by RT Mössbauer spectroscopy measurements on fresh SF, SFC6 and SFC15 samples (Table 2 and Fig. 3). These samples are paramagnetic at RT, and all contain $Fe^{4+}$ alongside with $Fe^{3+}$, even if some discussion is needed. In agreement with the above discussed XRD results, Mössbauer results showed that the structure of SF corresponds to $Sr_8Fe_8O_{23}$ (or $SrFeO_{2.87}$) and that our experimental spectra are identical to the literature [29]. Our interpretation (Fig. 2 and Table 2), however, is slightly different: we found octahedral, high spin $Fe^{4+}$, the unusual oxidation state $Fe^{3.5+}$ (very common in $SrFeO_{2.86}$) and a distorted $Fe^{3+}$ site respect an octahedral geometry, with distortion caused by either geometric reasons (tetragonal site) or by a coordinative insaturation (CN$<$6). If we assume that the unusual state (3.5+) is in fact a continuous electron exchange between $Fe^{4+}$ and $Fe^{3+}$, too fast for Mössbauer to be unequivocally determined, we can deduce the amount of $Fe^{4+}$ and $Fe^{3+}$ originally present in the sample. These data can be correlated with the amount on $Fe^{4+}$ and $Fe^{3+}$ found in SF6 and SFC15 (Fig. 2 and Table 2), for which the Mössbauer analysis showed octahedral high-spin $Fe^{4+}$ and octahedral $Fe^{3+}$ sites. This correlation is linear, and $Fe^{4+}$ decreases with the increase of cerium content, analogously to other A-site doped ferrates [4,11]. Apparently, thus, cerium is able to stabilize the formation of octahedral $Fe^{3+}$ (Table 2), suggesting a "preference"—for the doping element—for cubic environments vs. tetragonal ones (Table 1).

From Rietveld refinements, high microstrain parameter values have been obtained (between 6 and 12 Å). These unusual values could be essentially due to the presence of two different iron oxidation states. The crystallite size of the investigated powders decreases from 250 nm, in the pure strontium ferrate (SF), to 70–120 nm, in the Ce-doped samples (Table 1).

Differences in surface area and pore volume for different cerium doping content have been found by $N_2$ adsorption

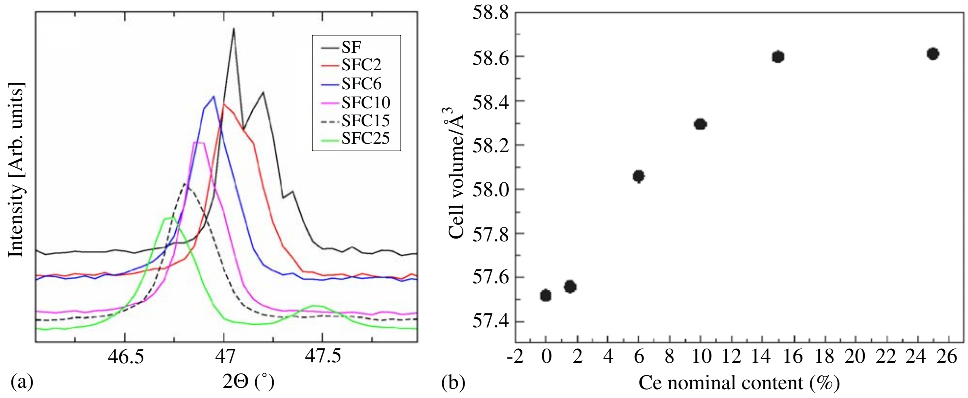

Fig. 2. (a) Expanded XRD pattern of Ce-doped strontium ferrates between 45.5 and 48.5°2$\theta$; (b) linear increasing of cell volume with cerium nominal content.

Table 2
Mössbauer parameters for SF, SFC6 and SFC15 samples

| | Assignment | $\delta$ (mm s$^{-1}$) | $\Delta^{a}$ or $2\varepsilon^{b}$ (mm s$^{-1}$) | $\Gamma$ (mm s$^{-1}$) | $H$ (T) | Spectral area (%) |
|---|---|---|---|---|---|---|
| SF | $Fe^{4+}$ | 0.055±0.002 | | 0.45±0.01 | | 39±1 |
| | $Fe^{3.5+}$(o) | 0.158±0.005 | 0.66±0.01 | 0.412±0.008 | | 56±1 |
| | $Fe^{3+}$ | 0.78±0.02 | 0.52±0.05 | 0.30±0.01 | | 5±1 |
| SFC6 | $Fe^{4+}$ | −0.049±0.001 | | 0.489±0.003 | | 65±1 |
| | $Fe^{3+}$(o) | 0.323±0.003 | | 0.546±0.008 | | 35±1 |
| SFC15 | $Fe^{4+}$ | −0.097±0.002 | | 0.555±0.007 | | 56±1 |
| | $Fe^{3+}$(o) | 0.437±0.004 | | 0.578±0.009 | | 44±1 |
| SFC6/He | $Fe^{3+}$(o) | 0.279±0.003 | −0.061±0.006 | 0.77±0.01 | 48.85±0.03 | 48±1 |
| | $Fe^{3+}$(t or p) | 0.162±0.005 | 0.103±0.009 | 1.35±0.01 | 41.8±0.1 | 52±1 |
| SFC15/He | $Fe^{3+}$(o) | 0.259±0.003 | −0.061±0.003 | 0.794±0.009 | 48.85±0.03 | 58±1 |
| | $Fe^{3+}$(t or p) | 0.142±0.002 | 0.04±0.01 | 1.28±0.02 | 41.8±0.1 | 42±1 |
| $SF/H_2$ | $Fe^{0}$ | −0.0067±0.0008 | 0.009±0.001 | 0.298±0.002 | 33.031±0.006 | 37±1 |
| | $Fe^{2+c}$ | 0.357±0.002 | 0.195±0.002 | 0.30±0.01 | | 11±1 |
| | $Fe^{3+}$ | 0.282±0.001 | −0.336±0.002 | 0.426±0.004 | 38.82±0.01 | 52±1 |
| $SFC15/H_2$ | $Fe^{0}$ | −0.102±0.001 | −0.002±0.002 | 0.303±0.003 | 33.011±0.007 | 36±1 |
| | $Fe^{2+c}$ | −0.460± | 0.54±0.01 | 1.1±0.2 | | 12±1 |
| | $Fe^{3+}$ | −0.52±0.01 | −0.02±0.01 | 1.35±0.02 | 35.06±0.08 | 52±1 |

[a] Quadrupole splitting (paramagnetic phase).
[b] Quadrupole splitting (magnetically ordered phase) o = octahedral; t = tetrahedral; p = penta-coordinated.
[c] $Fe^{2+}$ as FeO.

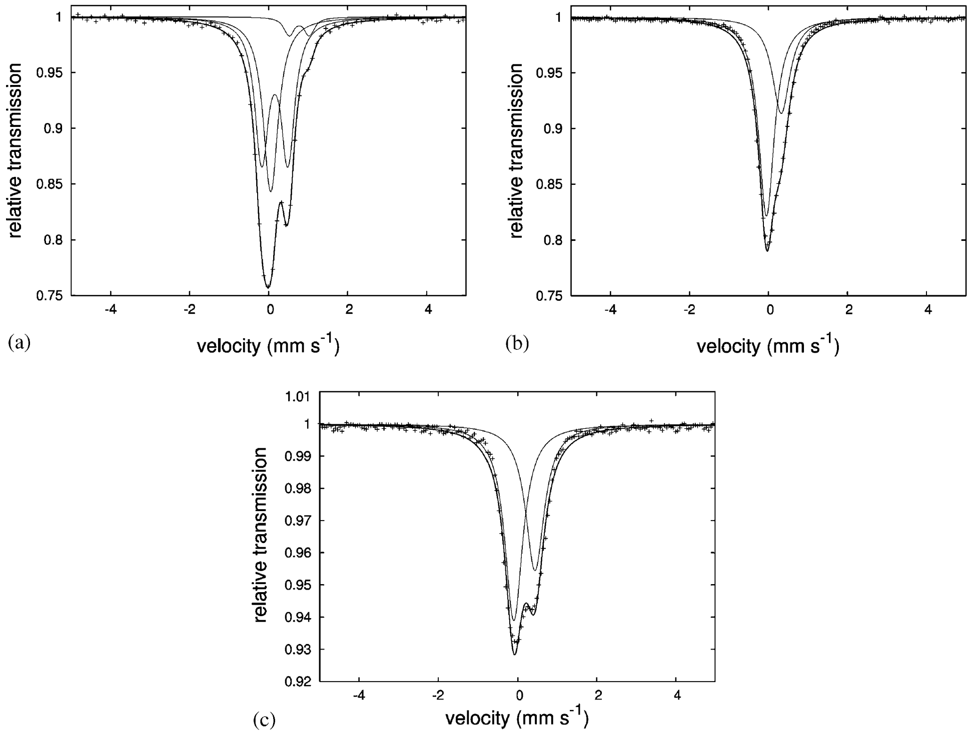

Fig. 3. Fits of Mössbauer spectra at RT for fresh SF (a), SFC6 (b) and SFC15 (c) samples: the fitted peak at lower $\delta$ value is related to $Fe^{4+}$ ions; the fitted peak at higher $\delta$ value to $Fe^{3+}$ ions.

measurements. For SF and SFC2, both surface area (≅10 m$^2$/g) and porosity (≅0.01 cm$^3$/g) are quite low; for higher Ce content, the surface area doubles and porosity increases up to 0.025 cm$^3$/g. SFC25, which contains 8 wt% of segregated $CeO_2$ shows the highest surface area (≅35 m$^2$/g) and pore volume (≅0.033 cm$^3$/g).

XPS quantitative results of the surface characterization of the samples are listed in Table 3. The relative chemical

Table 3
Binding energies (BE) of the XPS peaks and relative surface chemical composition of the investigated samples

| Sample | Sr 3d | O 1s | C 1s | Fe 2p | Ce 3d | |
|---|---|---|---|---|---|---|
| BE (eV) | 133.8 | 529.0 | 285.1 | 710.1 | 881.8 | Sr/Fe |
| SF | 11.4 | 39.3 | 39.3 | 10.0 | — | 1.1 |
| SFC6 | 7.3 | 25.4 | 61.5 | 5.8 | n. d. | 1.3 |
| SFC10 | 8.6 | 32.1 | 46.4 | 10.2 | 2.7 | 0.8 |
| SFC15 | 7.9 | 32.2 | 46.6 | 9.8 | 3.5 | 0.8 |
| SFC25 | 5.1 | 24.9 | 61.2 | 6.4 | 2.4 | 0.8 |
| SFC15/He | 11.0 | 42.0 | 31.4 | 12.6 | 2.9 | 0.9 |
| SFC15/$H_2$ | 14.1 | 44.2 | 29.6 | 8.7 | 3.4 | 1.6 |

Elemental concentrations are expressed as atomic percentage (atom. %).

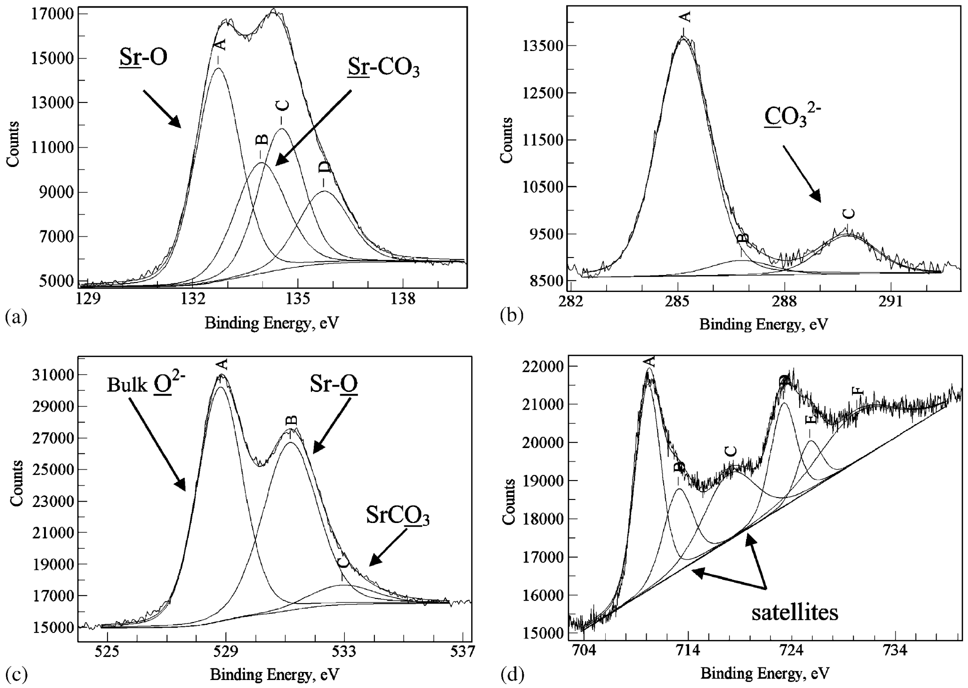

Fig. 4. XPS curve-fitting of the following photoelectron peaks: (a) Sr 3*d*, (b) C 1*s*, (c) O 1*s* and (d) Fe 2*p*. The scattered line refers to the raw data, while the solid line to the curve-fitting results.

composition is expressed as atomic percentage (at%). The surface (Sr/Fe) atomic ratio ranges from 0.8 to 1.3 for all the investigated as-prepared samples, as reported in Table 3. This (Sr/Fe) value corresponds to the stoichiometric bulk ratio (Sr/Fe = 0.85–1.00), at least within the experimental error. Representative XPS curve-fittings of the main photoelectron peaks in the samples are shown in Fig. 4. The Sr 3*d* region in Fig. 4a can be fitted by two doublets (Sr $3d_{3/2}$ and Sr $3d_{1/2}$) located at BE = 132.7 and 134.1 eV, which can be assigned to surface Sr–O and Sr–$CO_3$ species, respectively [30–32]. $SrCO_3$ formation on the surface is around 23–37% with respect to the total Sr peak area (taken as 100%) in the perovskite samples. By analyzing the samples composition as a function of the ageing time, an almost linear correlation between the carbonate amount formed on the surface and the time elapsed from the synthesis of the sample has been found (not shown). Freshly prepared samples are carbonate-free and the surface carbonate amount increases with time up to 30% after 1 month, as a result of interaction with air. These surface carbonate species can be easily removed from the sample by a mild temperature treatment. The presence of $SrCO_3$ species on the samples surface is also confirmed by the C 1*s* and O 1*s* peak fittings. C 1*s* spectra can be fitted by three components at BE = 285.1, 286.6 and 289.8 eV, which are attributable to aromatic hydrocarbons from surface contamination, alcohoxy ($CH_2O_x$) and surface $CO_3^{-2}$ groups, respectively [30–32], as shown in Fig. 4b. In all the samples, O 1*s* spectra consist of three components reported in Fig. 4c, located at BE = 529.0, 531.2 and 532.5 eV, which can be assigned to bulk oxide species ($O^{2-}$), surface Sr–O and Sr–$CO_3^{-2}$ groups, respectively [30,31].

The XPS region in the range 700–740 eV shown in Fig. 4d reveals the complex spectral features of the Fe 2*p* photoelectron peak. The multiplet splitting effect is responsible of the broadening of the peaks and the presence of satellites structures can be ascribed to shake-up processes [33]. The core-level Fe 2*p* spectrum consists of the typical spin-orbit doublet: Fe $2p_{3/2}$ and Fe $2p_{1/2}$, separated by 13.1 eV. The Fe $2p_{3/2}$ peak is centered at BE = 710.1 eV and shows satellite shake-up features. Since very close BE values are detected by XPS for $Fe^{2+}$ and $Fe^{3+}$ species, it is rather difficult to quantify their relative distribution [32]. The curve fitting result and the comparison with a pure sample of $Fe_2O_3$ powder taken as reference (see below the paragraph "$H_2$-treated powders") allow the assignment to the contemporary presence of $Fe^{2+}$ and $Fe^{3+}$ species for the corresponding core-level Fe $2p_{3/2}$ BEs [30–32]. Although Mössbauer results on fresh samples show also the presence of bulk $Fe^{4+}$ species, a partial iron reduction occurs during the experimental conditions (ultrahigh vacuum and X-ray irradiation) of XPS measurements, leading only to the detection of the more stable surface $Fe^{3+}$ and $Fe^{2+}$ oxidation state. This is not surprising since it is known in the literature that undoped [32,34] and doped [10] strontium ferrates loose oxygen under low oxygen partial pressure at around 600–700 °C, by forming structures which contain just $Fe^{3+}$. The same reduction probably occurred under vacuum at RT under XPS experimental conditions.

### 3.2. *He-treated powders*

When the samples have been treated under He at 1000 °C and cooled under the same atmosphere, some structural transformations occurred. For SF and SFC2 samples, XRD showed that orthorhombic brownmillerite-type structures have been formed (Fig. 5a and Table 4). Minor amounts of $Sr_4Fe_4O_{11}$ (Fig. 5a and Table 4) have been also detected, in agreement with the literature [35]. Our results for Ce content $\geqslant$ 6 mol % show that after high-temperature He treatment, the structure remains cubic (Fig. 5b,d) although $a_0$ expands from 3.861 to 3.884 Å, for the as-prepared samples (Table 1), to around 3.90 Å, for the He-treated samples (Table 4). When the powders are treated in He at high temperature, the microstrain parameter tends to decrease to around 4 Å for any Ce content, since only $Fe^{3+}$ is present. Crystallite size values do not change very much after this treatment (Table 4). Formation of cubic structures with expanded lattice has already been evidenced in literature for Pr and Bi-doped $SrFeO_3$, and it has been attributed to $Fe^{3+}$ formation under inert or reducing conditions [4,12]. In this work, $Fe^{3+}$ formation in the expanded phases has been confirmed by Mössbauer spectroscopy measurements on He-treated SFC6 and SFC15, which showed also that, after He treatment, no detectable amount of $Fe^{4+}$ was present. Moreover, the presence of two distinct magnetically ordered $Fe^{3+}$ sites was evidenced, an highly symmetric

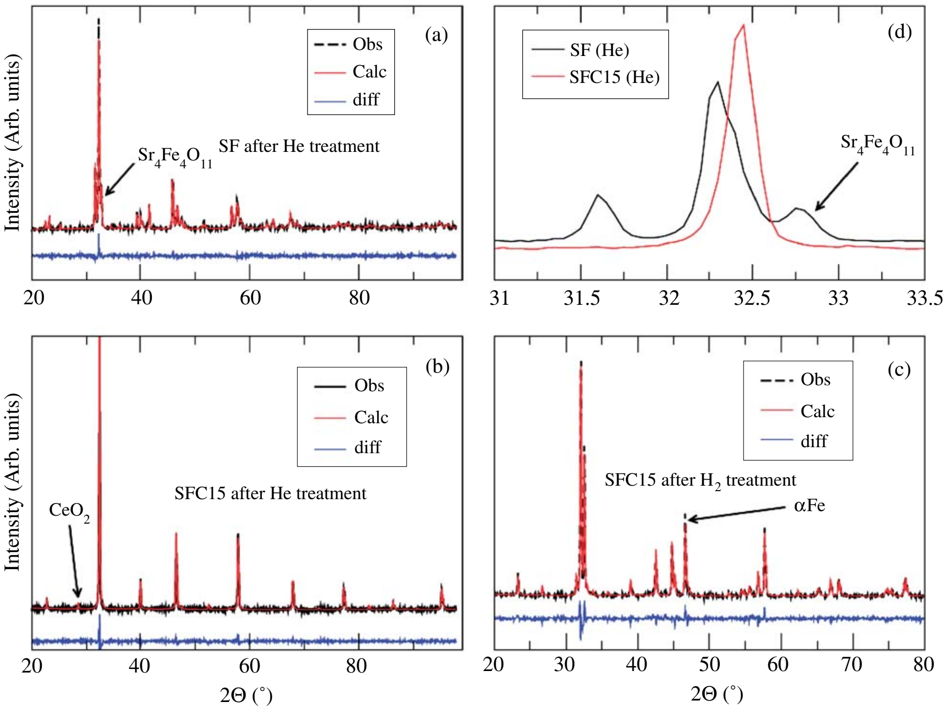

Fig. 5. Representative XRD structures of Ce-doped strontium ferrates after He or $H_2$ treatment: (a) Rietveld refinement of SF XRD pattern after He treatment with brownmillerite-type structure and some $Sr_4Fe_4O_{11}$; (b) Rietveld refinement of SFC15 XRD pattern after He treatment with cubic structure; (c) Rietveld refinement of SFV15 sample after $H_2$ treatment with Ruddlesden Popper $Sr_3Fe_2O_6$ structure and metallic iron; (d) enlargement of the SFC6 and SFC15 XRD patterns with different structures.

Table 4
Rietveld refinement results for He treated (after cooling from 1000 °C under He flow) $Sr_{1-a}Ce_aFeO_{3-x}$ samples with different Ce content

| Sample name | Phase composition [a] (% wt) | X-ray space group (structure) Cell parameters [b] (Å) | Crystal size (nm) | Agreements factors (%) |
|---|---|---|---|---|
| SF/He | $Sr_2Fe_2O_5$ (89.4(8))<br>$Sr_4Fe_4O_{11}$ (10.6(2)) | *Icmm* (orthorhombic)<br>$a_0 = 5.669$; $b_0 = 15.587$; $c_0 = 5.530$<br>*Cmmm* (orthorhombic)<br>$a_0 = 10.990$; $b_0 = 7.716$; $c_0 = 5.483$ | 177(5)<br>256(30) | $wR_p = 1.51$<br>$R_p = 1.20$<br>$R_F^2 = 8.23$ |
| SFC2/He | $Sr_{2(1-a)}Ce_{2a}Fe_2O_5$ (84.4(1))<br>$Sr_4Fe_4O_{11}$ (15.6(4)) | *Icmm* (orthorhombic)<br>$a_0 = 5.658$; $b_0 = 15.626$; $c_0 = 5.532$<br>*Cmmm* (orthorhombic)<br>$a_0 = 11.013$; $b_0 = 7.732$; $c_0 = 5.494$ | 173(10)<br>101(10) | $wR_p = 1.83$<br>$R_p = 1.35$<br>$R_F^2 = 7.79$ |
| SFC6/He | $Sr_{0.94}Ce_{0.06}FeO_{3-x}$ (100) | *Pm3m* (cubic)<br>$a_0 = b_0 = c_0 = 3.909$ | 124(10) | $wR_p = 2.35$<br>$R_p = 1.60$<br>$R_F^2 = 6.10$ |
| FC10/He | $Sr_{0.90}Ce_{0.10}FeO_{3-x}$ (100) | *Pm3m* (cubic)<br>$a_0 = b_0 = c_0 = 3.902$ | 76(5) | $wR_p = 2.21$<br>$R_p = 1.43$<br>$R_F^2 = 5.87$ |
| FC15/He | $Sr_{0.85}Ce_{0.15}FeO_{3-x}$ (99.0(2))<br>$CeO_2$ (<1) | *Pm3m* (cubic)<br>$a_0 = b_0 = c_0 = 3.901$ | 86(5) | $wR_p = 2.23$<br>$Rp = 1.55$<br>$R_F^2 = 8.11$ |
| C25/He | $Sr_{0.85}Ce_{0.15}FeO_{3-x}$ (91.3(2))<br>$CeO_2$ (8.7(1)) | *Pm3m* (cubic)<br>$a_0 = b_0 = c_0 = 3.899$ | 85(5) | $wR_p = 1.79$<br>$R_p = 1.32$<br>$R_F^2 = 3.80$ |

bis Rietveld refinement results for $H_2$ treated (after TPR and cooling from 1000 °C under He flow) $Sr_{1-a}Ce_aFeO_{3-x}$ samples with 0 and 15 mol% Ce

| | | | | |
|---|---|---|---|---|
| $SF/H_2$ | $Sr_3Fe_2O_6$ (88(2))<br>Fe (12(3)) | *I*4/*mmm* (Tetragonal)<br>$a_0 = b_0 = 3.892$; $c_0 = 20.038$<br>*Im* − 3*m* (Cubic)<br>$a_0 = b_0 = c_0 = 2.864$ | 100(5)<br>110(10) | $wR_p = 2.60$<br>$R_p = 1.98$<br>$R_F^2 = 6.87$ |
| $SFC15/H_2$ | $Sr_{3(1-a)}Ce_{3a}Fe_2O_6$ (83.3(1))<br>$CeO_2$ containing $Sr_3Fe_2O_6$ (5.6(5))<br>Fe (11.1(3)) | *I*4/*mmm* (Tetragonal)<br>$a_0 = b_0 = 3.901$; $c_0 = 20.096$<br>*I*4/*mmm* (Tetragonal)<br>$a_0 = b_0 = 3.852$; $c_0 = 21.232$<br>*Im* − 3*m* (Cubic)<br>$a_0 = b_0 = c_0 = 2.867$ | 106(5)<br>79(10)<br>126(10) | $wR_p = 2.67$<br>$R_p = 1.76$<br>$R_F^2 = 8.93$ |

[a] "a" values are deduced from the nominal Ce content and from the phase composition.
[b] Standard deviation for cell parameters is ±0.003 Å.

octahedral one (characterized by an higher hyperfine magnetic field) and another one, with lower coordination number (probably 4) (Table 2). These results are very similar to those obtained for Pr-doped $SrFeO_3$, although in the literature the contribution of tetra-coordinated iron is separated from that of penta-coordinated iron [12]. The octahedral/tetrahedral ratio increases with Ce content (Fig. 6 and Table 2), similarly to what has been reported in the literature for La-doped strontium ferrates [10]. From Table 2, by comparing the results for fresh and He-treated samples, it is easy to deduce that $Fe^{3+}$ with coordination lower than 6 probably originates from reduction of $Fe^{4+}$, which gives rise to around 80% of $Fe^{3+}$ with coordination lower than 6 and to around 20% of octahedral $Fe^{3+}$, whereas octahedral iron was already present in the fresh samples and now is incremented of around 20%. This fact, according to the original hypothesis that cerium stabilizes the octahedral site of $Fe^{3+}$ in the fresh samples, leads to affirm that cerium also determines the fraction of octahedral $Fe^{3+}$ present in the system after He treatment. From these observations and from the previously discussed XRD results, it may be concluded that when the octahedral $Fe^{3+}$ concentration in the fresh samples reaches 35 mol%, the structure of the fresh samples is cubic and a brownmillerite-type phase formation is surely hindered, at the condition that cerium is present as dopant to stabilize the cubic structure (Table 2). Cerium effect on Ce-doped strontium ferrates could be mainly ascribed to an interaction between the redox couples $Ce^{4+}$–$Ce^{3+}$ and $Fe^{4+}$–$Fe^{3+}$ in the solid solution, which are in contact through oxygen bridges. It is worth noticing that in La-doped $SrFeO_3$, where La possess only one oxidation state ($La^{3+}$), brownmillerite-type structure has been reported to form under low oxygen pressure thermal treatment [10],

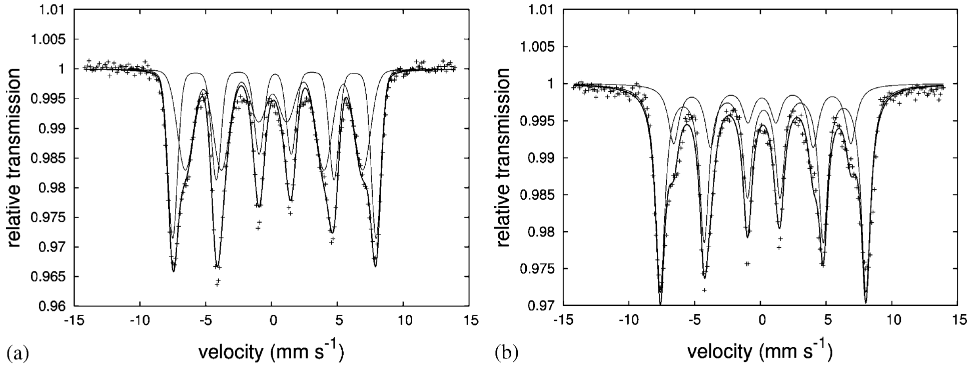

Fig. 6. Fits of Mössbauer spectra of (a) SFC6 and (b) SFC15 samples after He treatment: the sextet at higher magnetic field is due to octahedral $Fe^{3+}$; the sextet at lower magnetic field is due to $Fe^{3+}$ in a lower coordination.

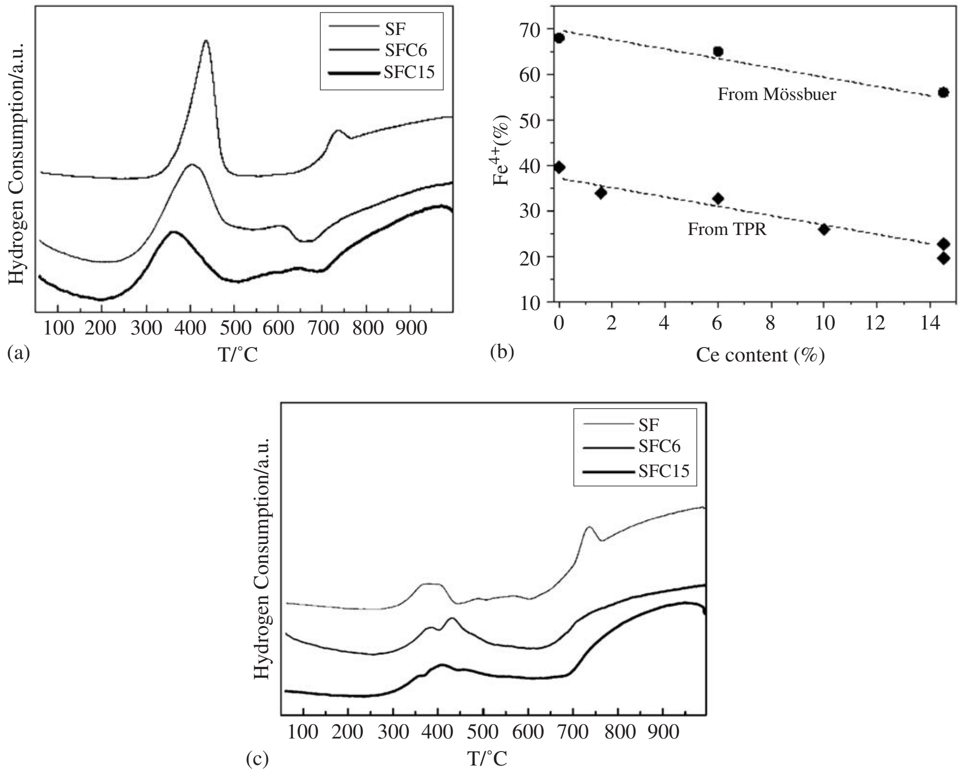

Fig. 7. TPR profiles for some representative $Sr_{1-a}Ce_aFeO_{3-x}$ samples: (a) TPR (1st cycle); (b) linear correlation vs. cerium content of the $Fe^{4+}$ mol% deduced from the first TPR peak compared with $Fe^{4+}$ mol% deduced from Mössbauer; (c) TPR (2nd cycle) after reoxidation at 1000 °C.

whereas other cations, like praseodymium and bismuth, that can change quite easily between two oxidation states, behaves quite similarly to cerium [4,12]. We may exclude that formation of cubic expanded phases depends on the ionic radius of the dopant, since $Ce^{3+}$ and $La^{3+}$ have very similar ionic radius, and, on the other side, $Bi^{3+}$, which is able to form cubic expanded phases, has lower ionic radius than $Ce^{3+}$ [26]. From another point of view, we believe also that the excess of oxygen atoms in the crystal structure, caused by Ce doping through the oxygen vacancy suppression, hinders the formation of ordered brownmillerite-type phase, as other authors observed for similar systems [36].

From TPR profiles, information has been obtained on the He-treated or partially treated samples: the first TPR has been acquired after an oxidation pre-treatment at 500 °C, followed by a cooling under inert gas flow, whereas the second TPR has been acquired after reoxidation at 1000 °C and He-cooling to RT. TPR profiles show two main groups of peaks (Fig. 7a): the first group (low-$T$ peaks) between 300 and 500 °C and the second one (high $T$ peaks) between 700 and 1000 °C.

According to the literature [32], the low-$T$ peaks represent the $H_2$ amount required to reduce all the $Fe^{4+}$ ions to $Fe^{3+}$ ions in two consecutive steps. In particular, after the first step, a mixed-valence perovskite-type structure is formed, whereas at the end of the second step, a brownmillerite-type structure is obtained for the undoped strontium ferrate [32]. According to our results on He-treated samples (Table 4 and Fig. 5a,b,d), it is reasonable to infer that during the TPR experiment, at the end of the low-*T* peaks, brownmillerite-type structure forms only for SF and SFC2 samples, while for the other Ce-doped samples the cubic expanded phases is obtained. Moreover, from Fig. 7a and Table 5, we observe that the first TPR peak's area, decreases with Ce doping. From the first TPR peak's area, it is easy to calculate the correspondent $Fe^{4+}$ percentage, which results in linear correlation with Ce content (Fig. 7b). The trend depicted in Fig. 7b is in agreement with the previously shown Mössbauer observations (Table 2) that $Fe^{4+}$ decreases with Ce doping. Nevertheless the $Fe^{4+}$ values in SF, SFC6 and SFC15 calculated from the first TPR peak are all systematically lower than the values calculated from Mössbauer measurements (Fig. 6b). If strontium ferrates would contain only $Fe^{4+}$, the theoretical amount of $H_2$ should correspond to around 59 mL $H_2$/g (equivalent to the reduction of 1 g of $SrFeO_3$ by a 1 electron-process). It is known, however, from the literature [37,38] and confirmed by our Mössbauer results (Table 2) that even the undoped strontium ferrate, $Sr_8Fe_8O_{23}$, contains around 70% of $Fe^{4+}$. Hence, we should expect for SF sample that at least a 70% fraction of 59 mL $H_2$/g (43 mL/g) has been consumed in the first TPR peak. It is quite clear that some iron reduction already occurred during the pretreatment when, after the oxidation treatment at 500 °C, the sample has then been cooled down under inert gas flow from 500 °C to RT. Although we have already shown that our samples are reduced under He flow at 1000 °C, there is some evidence in the literature that evolution of oxygen starts already at around 400 °C [32].

Finally, the reduction temperature of the first TPR peak decreases from about 440 to 350 °C for increasing Ce content (Table 5 and Fig. 7a). We exclude in the first TPR peak a contribution of $Ce^{4+}$ which reduces to $Ce^{3+}$. This reduction will probably occur at higher temperatures, similarly to the bulk $CeO_2$ [39]. TPR profiles of SFC6 and SFC15 samples show the appearance of some small peaks between 500 and 700 °C, probably due to some easily available oxygen, created by lattice perturbation for Ce doping, as described in literature for non-stoichiometric $LaFeO_3$ [40].

Table 5
$H_2$ uptake (±15%) consumed in the TPR experiment (1st and 2nd cycle) by $Sr_{1-a}Ce_aFeO_{3-x}$ samples with different Ce content

| | 1st TPR cycle ml $H_2$/g low-*T* peaks | 1st TPR cycle ml $H_2$/g high-*T* peaks | 2nd TPR cycle [a] ml $H_2$/g high-*T* peaks |
|---|---|---|---|
| Sample name | | | |
| SF | 23 (437 °C) | 52 | 52 |
| SFC2 | 20 (415 °C) | 46 | 46 |
| SFC6 | 19 (403 °C) | 32 | 34 |
| SFC10 | 15 (375 °C) | 32 | 33 |
| SFC15 | 12 (365 °C) | 43 | 43 |
| SFC25 | 12 (346 °C) | 43 | 45 |

Temperature values in brackets refer to the maximum of the indicated reduction peak.

[a] The low-*T* peaks of the 2nd TPR cycle are all around 5 ml $H_2$/g and have not been reported in the table.

The high-temperature TPR peaks (700–1000 °C) represent the $H_2$ amount consumed in the reduction of $Fe^{3+}$ to $Fe^{2+}$ and eventually to $Fe^0$. For pure SF and SFC2 samples, TPR profiles are very similar to those in the literature, but for the other Ce-doped strontium ferrates, some significant differences have been observed. In SFC6 and SFC15 (Fig. 7a), the peak around 700 °C disappeared, indicating that it is probably related with the $Fe^{3+}$ reduction in brownmillerite-type structure to $Fe^{2+}$. Moreover the $H_2$ uptake (mL/g) in the second TPR peak group should be equal to the theoretical value necessary to reduce all the $Fe^{3+}$ to $Fe^0$ (3 electron process = 3 × 59 mL $H_2$/g), but the observed value is considerably lower (Table 5), since the reduction does not complete at 1000 °C (Fig. 7a), as already found for $LaFeO_3$ [41].

The second TPR cycle, which occurs after a reoxidation at 1000 °C followed by cooling from 1000 °C to RT under inert gas flow, shows some different features (Fig. 7c): the low TPR peaks almost disappear, indicating that only some residual $Fe^{4+}$ remains, as found in the literature for $LaFeO_3$, which should contain only $Fe^{3+}$ [40,41]. The $H_2$ volume consumed in the second TPR peak group remains unchanged from the first TPR to the second TPR cycle (Fig. 7a,c and Table 5), demonstrating that the reduction process was totally reversible.

The TPO experiments after TPD give us an indication on the reoxidation of the phase (brownmillerite-type or expanded) which is formed after TPD as well as on the oxygen adsorption capacity of the investigated samples. In Fig. 8a, the TPO curve of a representative sample (SFC6) is shown. The reoxidation peak starts at 100 °C and is complete at 350 °C. The TPD–TPO process is totally reversible. In Fig. 8b, the mL $O_2$ consumed in the TPO process have been correlated with the Ce content: oxygen consumption increases from 0 until 6 mol% (17 mL $O_2$/g), but then decreases again for higher Ce content. This trend can be explained by the concurrence of two effects: the decrease of oxygen vacancies with increasing Ce content for the formation of the cubic expanded disordered phase, and the increased oxygen mobility due to stabilization of $Fe^{3+}$ in the octahedral coordination. When the oxygen vacancies are decreased too much, like in SFC15, the advantage of the geometric effect of iron coordination cannot compensate any more the decrease of vacancies, and the interaction with oxygen decreases consequently. Previous studies by Trofimenko and Ullmann [14] demonstrated similar trend for Ce-doped $SrFe_{0.8}Co_{0.2}O_3$ in electronic conductivity which decreased for Ce contents higher than 5 mol%, suggesting that the oxygen consumption in these materials could be controlled by the electronic conductivity of the system.

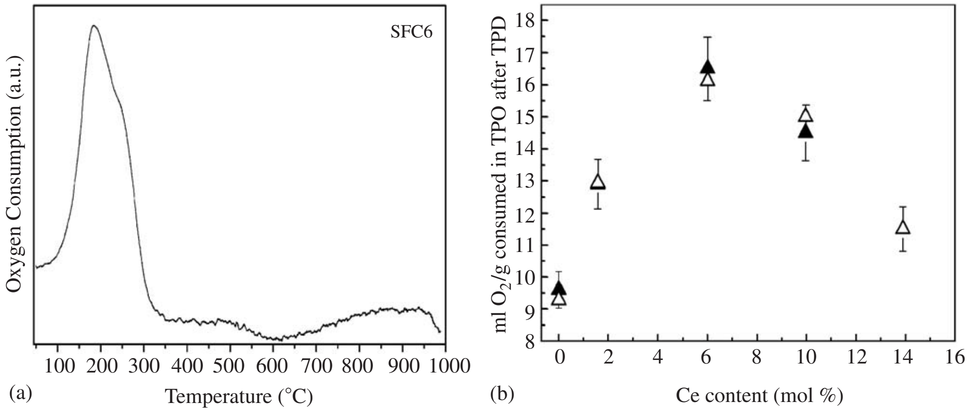

Fig. 8. (a)TPO after TPD curve for SFC6 as a representative $Sr_{1-a}Ce_aFeO_{3-x}$ sample. (b) $O_2$ consumption values in ml $O_2$/g (from TPO after TPD) vs. Ce content. The black or white triangles refer to the two different TPD–TPO cycles.

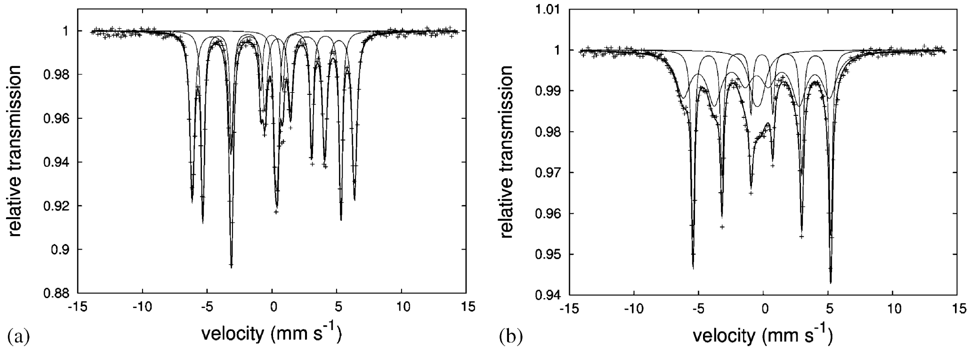

Fig. 9. Fits of Mössbauer spectrum of (a) SF and (b) SFC15 samples after H2 treatment: the sharper sextet is metallic α-Fe; the other two sub-spectra are from $Fe^{3+}$ (less sharp sextet) and from $Fe^{2+}$(central sub-spectrum).

### 3.3. $H_2$-treated powders

The phase composition of an undoped and a Ce-doped samples after TPR (by cooling the sample under He) has been investigated in details by XRD, Mössbauer and XPS measurements. XRD analysis shows that the main phase composition of SF and SFC15 after TPR consists of a Ruddlesden Popper (RP) phase of the type $Sr_3Fe_2O_6$ and some metallic iron (Fig. 5c and Table 4bis). Although some authors found that for undoped strontium ferrate only FeO and SrO and finally metallic iron are formed at the end of the reduction process [32], in this work, in the reduced SF sample, the RP phase was detected, in agreement with other authors [42]. RP phases derived from perovskite-type structure and are formed by alternating layers of $ABO_{3-x}$ and oxide of the A cation [34]. In the SF sample, the cell parameter of the RP phase (Table 4bis) is in agreement with the literature [43]. In SFC15, the presence of cerium as a dopant could be responsible for the slightly larger cell parameters (Table 4bis) with respect to the literature (3.901 Å vs. 3.894 Å for $a_0$ and $b_0$; 20.096 Å vs. 20.039 Å for $c_0$). Few percent of an additional RP phase are also present in SFC15 sample, as it is demonstrated by XRD analysis in Table 4bis, and it is reasonable to consider it as the result of the interaction, under reducing conditions, of $SrFeO_3$ with the 1 wt% segregated $CeO_2$ phase. This hypothesis is supported by the experimental observations that in SFC15, the $CeO_2$ XRD peak disappeared after reduction and appeared again after reoxidation (data not shown) and that in SF this additional RP phase is absent (Table 4bis). Mössbauer results seem to substantially confirm XRD results: SF and SFC15 contain mainly $Fe^{3+}$, which is very probably square pyramidal [43], and metallic iron. From Mössbauer results, some $Fe^{2+}$ was also present (Table 2 and Fig. 9), probably as FeO. Since FeO was not evidenced by XRD, it is probably amorphous or very well dispersed. Nevertheless some differences are evident by comparing the two spectra in Fig. 9a and b. In SFC15, quite large $\Gamma$ values suggest a larger distortion in the structure symmetry. This perturbation could be provoked by the introduction of cerium in the RP phase. Regarding metallic α-iron, a quantitative comparison between the two techniques was not possible due to the phase separation occurring after the reduction, which misleads Mössbauer results overestimating metallic iron.

The XPS analysis performed on the SFC15 sample after TPR evidences the presence of metallic iron on the surface. Fe 2$p$ spectra in the SFC15 sample, both before and after

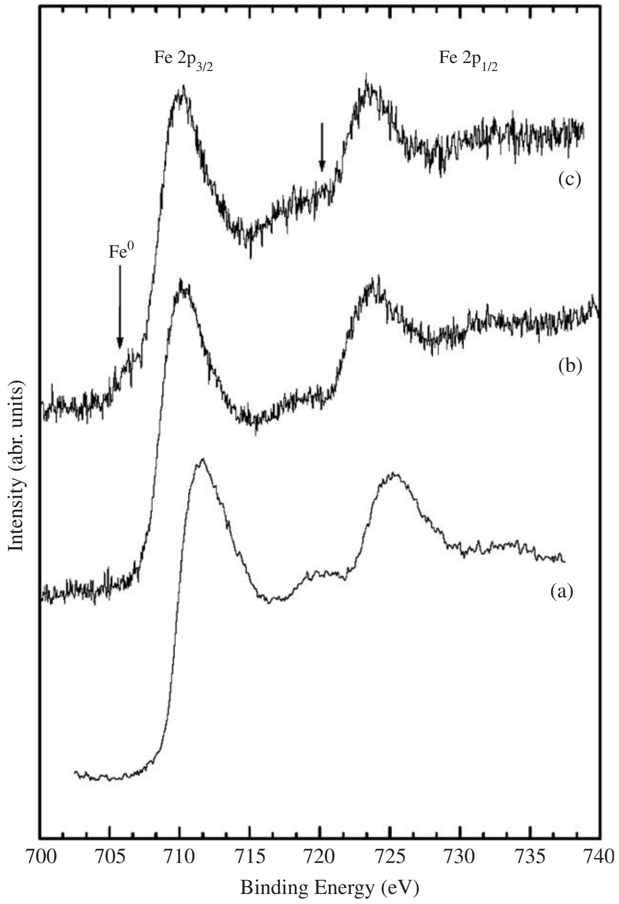

Fig. 10. XPS spectra in the Fe $2p$ region: curve (a) the XPS spectrum of $Fe_2O_3$ taken as reference; curve (b) SFC15 sample before and curve (c) after TPR ($H_2$ treatment).

TPR ($H_2$ treatment), are shown respectively in the curve b and curve c of Fig. 10. The only difference in these Fe $2p$ spectra is represented by the small shoulder at the low BE side of the spectrum in curve c. This feature can be fitted by a Fe $2p_{3/2}$ component at $BE = 706.5\,eV$, which can be assigned to $Fe^0$ species [30,31], as also confirmed by the Fe $2p_{1/2}$ doublet component indicated by an arrow in curve c. The surface modifications underwent by the SFC15 sample upon the TPR treatment are reported in Table 3, showing an higher Sr/Fe ratio due to a higher Sr content in the surface, which indicates the presence of $Sr_3Fe_2O_6$ on the surface.

### 3.4. Preliminary electrochemical impedance results

In Fig. 11, the Log (ASR) vs. $1000/T$(K) has been reported for 3 different Ce content (0, 6 and 15 mol%). The highest ASR has been measured for SF, the lowest one for SFC6, whereas SFC15 lays in between. From this trend and from the TPO trend of Fig. 8b, we may tentatively conclude that the oxygen adsorption could be considered as the rate determining step of the oxygen reduction process in Ce-doped $SrFeO_3$.

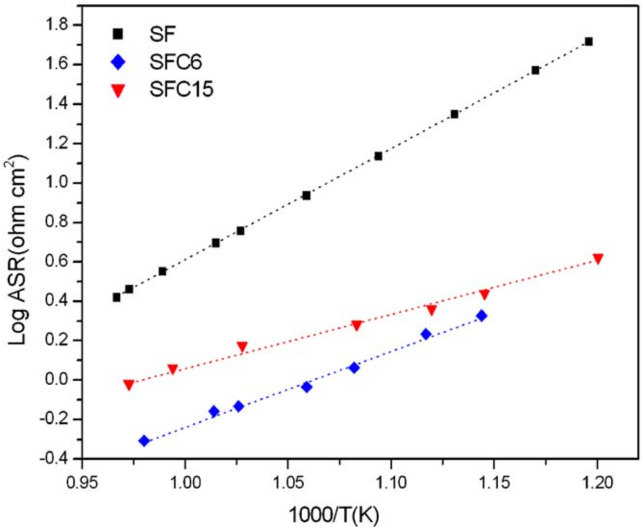

Fig. 11. Log (ASR) vs. $1000/T$(K) for SF, SFC6 and SFC15 taken from preliminary E IS experiments.

## 4. Conclusions

In this work, structure–properties relationships of Ce-doped $SrFeO_3$ prepared by citrate–nitrate auto-combustion synthesis have been investigated to evaluate the effect of Ce-doping in the structure, phase stability, reducibility and interaction of these materials with oxygen.

Our results show that citrate–nitrate smoldering auto-combustion method is effective in obtaining single-phase $Sr_{1-a}Ce_aFeO_{3-x}$ $(0 \leqslant a < 0.15)$ powders, with a surface area of $\cong 20\,m^2/g$ and a crystallite size of $\cong 100\,nm$. Structural and reduction properties of cerium-doped strontium ferrates are greatly improved by Ce substitution and are highly dependent on cerium concentration in the solid solution. The $Sr_{1-a}Ce_aFeO_{3-x}$ structure is cubic only for $a \geqslant 0.06$, while for $a < 0.06$ remains tetragonal. Moreover, for $a \geqslant 0.06$ after semi-reductive treatment under inert gas, an expanded cubic phase is obtained instead of the less conducting brownmillerite-type structure. The improved properties are mainly correlated with the stabilization of octahedral $Fe^{3+}$ site and cubic environment operated by cerium doping. This stabilization occurs probably through an interaction between the redox couples $Ce^{4+}$–$Ce^{3+}$ and $Fe^{4+}$–$Fe^{3+}$ connected in the solid solution by oxygen bridges. In the presence of cerium, when the octahedral iron concentration in the fresh samples is around 35%, expanded cubic phases are favored after He treatment at high temperatures and brownmillerite-type phase formation is hindered. The reduction temperature of $Fe^{4+}$ to $Fe^{3+}$ in Ce-doped $SrFeO_3$ decreases with Ce doping. During the reduction process of Ce-doped $SrFeO_3$ at high temperatures, formation of RP phase occurs, where cerium is inserted in the RP structure.

The best results in TPO (after TPD) experiments have been obtained for $a = 0.06$, whereas for higher Ce content, the beneficial geometric effect of octahedral iron cannot compensate the gradual suppression of oxygen vacancy concentration induced by Ce. Preliminary EIS results showed that the lowest ASR has been obtained for the same cerium content (6 mol%). Oxygen adsorption has been identified as the rate determining factor of the overall cathode process in Ce-doped strontium ferrates. All these findings are important for the application of Ce-doped $SrFeO_3$ materials in low-temperature oxygen-conducting devices. Further experiments on the electrochemical properties of these materials are in progress.

## Acknowledgments

The authors are thankful to Prof. G. Deganello for important suggestions. Moreover the Italian Ministry of Foreign Affairs (MAE), under the frame of the Italy–Japan Joint Lab on "Nanostructured Materials for Environment and Energy" (NaMaTEE), is greatly acknowledged for supporting the preliminary impedance tests.

## References

[1] C. Liang, D. Yang, Z. Yang, F. Hou, M. Xu, Surf. Coatings Technol. 200 (2005) 2515–2517.
[2] V.P.S. Awana, J. Nakamura, J. Lindén, M. Karpinnen, H. Yamauchi, Solid State Commun, 119 (2001) 159–162.
[3] Y.M. Zhao, X.J. Yang, Y.F. Zheng, D.L. Li, S.Y. Chen, Solid State Commun. 115 (2000) 365–368.
[4] S. Zongping, Y. Cong, G. Xiong, S. Sheng, W. Yang, Sci. China (Series B) 43 (2000) 421–427.
[5] M.T. Colomer, B.C.H. Steele, J.A. Kilner, Solid State Ionics 147 (2002) 41–48.
[6] H. Ullmann, N.E. Trofimenko, F. Tiez, D. Stöver, A. Ahmad-Khanlou, Solid State Ionics 138 (2000) 79–90.
[7] A. Mai, V.A.C. Haanappel, S. Uhlenbruck, F. Tietz, D. Stöver, Solid State Ionics 176 (2005) 1341−1350.
[8] A.A. Leontiou, A.K. Ladavos, T.V. Bakas, T.C. Vaimakis, P.J. Pomonis, Appl. Catal. A: Gen. 241 (2003) 143–154.
[9] S. Shin, M. Yonemura, H. Ikawa, Mater. Res. Bull. 13 (1978) 1017–1021.
[10] M.V. Patrakeev, J.A. Bahteeva, E.B. Mitberg, I.A. Leonidov, V.L. Kozhevnikov, K.R. Poeppelmeier, J. Solid State Chem. 172 (2003) 219–231.
[11] S.E. Dann, D.B. Currie, M.T. Weller, M.F. Thomas, A.D. Al-Rawwas, J. Solid State Chem. 109 (1994) 134–144.
[12] M. Stange, J. linden, A. kjekshus, N. binsted, M.t. weller, B.c. hauback, H. fjellvag, J. Solid State Chem. 173 (2003) 148–163.
[13] Y.D. Tretyakov, V.V. Sorokin, A.R. Kaul, A.P. Erastova, J. Solid State Chem. 18 (1976) 253–261;
H.N. Pandya, R.G. Kulkarni, P.H. Parsania, Mater. Res. Bull. 25 (1990) 1073–1077;
M. Robbins, G.K. Wertheim, A. Menth, R.C. Sherwood, J. Phys. Chem. Solids 30 (1969) 1823–1825.
[14] N.E. Trofimenko, H. Ullmann, J. Eur. Ceram. Soc. 20 (2000) 1241–1250.
[15] N.E. Trofimenko, H. Ullmann, J. Paulsen, R. Mueller, Solid State Ionics 99 (1997) 201–214.
[16] R.N. Basu, F. Tietz, E. Wessel, H.P. Buchkremer, D. Stover, Mater. Res. Bull. 39 (2004) 1335–1345.
[17] S.B. Adler, Chem. Rev. 104 (2004) 4791–4843.
[18] F. Deganello, G. Deganello, unpublished work.
[19] A.C. Larson, R.B. Von Dreele, LANSCE, MS-H 805, Los Alamos National Laboratory, Los Alamos, NM 87545, USA, 1998.
[20] L.B. McCusker, R.B. Von Dreele, D.E. Coxd, D. Louer, P. Scardi, J. Appl. Crystallogr. 32 (1999) 36–50.
[21] Y.M. Zhao, M. Hervieu, N. Nguyen, B. Raveau, J. Solid State Chem. 153 (2000) 140–144.
[22] M.P. Seah, in: X. Briggs and X. Seah (Eds.), Practical Surface Analysis, second ed., vol. 1, Wiley, Chichester, 1990, p. 202.
[23] C.D. Wagner, L.E. Davis, W.M. Riggs, Surf. Interface Anal. 2 (1980) 53–55.
[24] S. Brunauer, P.H. Emmet, E. Teller, J. Am. Chem. Soc. 60 (1938) 309–319.
[25] E.P. Barret, L.G. Joyner, P.P. Halenda, J. Am. Chem. Soc. 73 (1951) 373–380.
[26] J.P. Hodges, S. Short, J.D. Jorgensen, X. Xiong, B. Dabrowski, S.M. Mini, C.W. Kimball, J. Solid State Chem. 151 (2000) 190–209.
[27] J.-F. Huang, X. Ni, J.-C. Bao, J.-H. Wu, Jiegon Huaxue 13 (1994) 350–359.
[28] R.D. Shannon, Acta Crystallogr. A 32 (1976) 751–767.
[29] P.K. Gallagher, J.B. MacChesney, D.N.E. Buchanan, J. Chem. Phys. 41 (1964) 2429–2434;
L. Fournes, Y. Potin, J.C. Grenier, G. Demazeau, M. Pouchard, Solid State Commun. 62 (1987) 239–244;
M. Takano, N. Okita, N. Nakayama, Y. Bando, Y. Takeda, O. Yamamoto, J.B. Goodenough, J. Solid State Chem. 73 (1988) 140–150.
[30] J.F. Moulder, W.F. Stickle, P.E. Sobol, K.D. Bomben, in: J. Chastain Jr., R.C. King (Eds.), Handbook of X-ray Photoelectron Spectroscopy, Phys. Electronics Inc., Eden Prairie, USA, 1995.
[31] P.A.W. Van der Heide, Surf. Interface Anal. 33 (2002) 414–425.
[32] H. Falcon, J.A. Barbero, J.A. Alonso, M.J. Martinez-Lope, J.L.G. Fierro, Chem. Mater. 14 (2002) 2325–2333;
C.-T. Wang, S.-H. Ro, J. Non-Cryst. Solids 352 (2006) 35–43.
[33] A.P. Grosvenor, B.A. Kobe, M.C. Biesinger, N.S. McIntyre, Surf. Interface Anal. 36 (2004) 1564–1574.
[34] M.V. Patrakeev, I.A. Leonidov, V.L. Kozhevnikov, V.V. Kharton, Solid State Sci. 6 (2004) 907–913.
[35] C. Haavik, T. Atake, H. Kawaji, S. Stolen, Phys. Chem. Chem. Phys. 3 (2001) 3863–3870.
[36] F. Prado, N. Grunbaum, A. Caneiro, A. Manthiram, Solid State Ionics 167 (2004) 147–154.
[37] K.V. Pokholok, I.A. Presnyakov, V.A. Ketsko, N.N. Oleinikov, N.T. Kuznetsov, Russ. J. Coord. Chem. 27 (2001) 632–635.
[38] G. Shirane, E.D. Cox, S.L. Ruby, Phys. Rev. 125 (1962) 1158–1165.
[39] A.M. Venezia, G. Pantaleo, A. Longo, G. Di Carlo, M.P. Casaletto, L.F. Liotta, G. Deganello, J. Phys. Chem. B 109 (2005) 2821–2827.
[40] R. Spinicci, A. Tofanari, A. Del Mastro, D. Mazza, S. Ronchetti, Mater. Chem. Phys. 76 (2002) 20–25.
[41] F.J. Berry, J.R. Gancedo, J.F. Marco, X. Ren, J. Solid State Chem. 177 (2004) 2101–2114.
[42] M. Wyss, A. Reller, H.R. Oswald, Solid State Ionics 101–103 (1997) 547–554.
[43] S.E. Dann, M.T. Weller, D.B. Currie, J. Solid State Chem. 97 (1992) 179–185.